Analyst

PAPER

View Article Online
View Journal



Cite this: DOI: 10.1039/c7an00446j

# Controllable Mn-doped ZnO nanorods for direct assembly of a photoelectrochemical aptasensor

Jing Li,[a,b] Zhihui Dai *[a] and Hongbo Li*[b]

A label-free photoelectrochemical (PEC) aptasensor for $K^+$ was first constructed by direct self-assembly of the $K^+$ aptamer onto the electrodeposited Mn-doped ZnO nanorods. In the presence of $K^+$, the conformation of G-quadruplex changes to a $K^+$-stabilized conformation, which can efficiently prevent the quercetin electron donor from reaching the functionalized photoanode, thus proportionately affecting the quercetin-enhanced photocurrent response. Under the optimal experimental conditions, the fabricated biosensor exhibited a linear response in the $K^+$ concentration range of 0.012 to 12.32 nmol $L^{-1}$, with a detection limit of 4.0 pmol $L^{-1}$, which was 3–5 orders of magnitude lower than that of most of the recently reported methods. The presence of other ions did not interfere with the detection of $K^+$, and the results in serum samples agreed well with those obtained by ICP-MS. Using $K^+$ as the detection model, this novel PEC aptasensor exhibited a good performance in terms of ultrasensitivity, selectivity and simplicity, and it was economical. As regards the electrode modification, this work provided a convenient direct self-assembly strategy that did not require the use of ionic polymers such as PDDA as a binder. Thus, this study paves the way for the immobilization of molecular probes for label-free PEC aptasensing.

Received 14th March 2017,
Accepted 4th May 2017

DOI: 10.1039/c7an00446j

rsc.li/analyst



## 1 Introduction

Potassium is an important cation in biology, and plays diverse roles in biological processes.[1] Abnormal $K^+$ fluctuations are a hallmark of diseases such as diabetes, AIDS, cancer, *etc*.[2] Thus, the detection of $K^+$ is very important for the early identification and diagnosis of these diseases. Among various detection methods, G-quadruplex-based aptasensors are more attractive for their good sensitivity and excellent selectivity. There are many robust aptasensors of $K^+$ reported to date (see Table 1), which often need particular nanomaterials such as Au nanoparticles or redox indicators such as a Fc label to transduce the signal. Therefore, a more simple, label-free and economical method remains a challenge.

Photoelectrochemical (PEC) bioanalysis has elicited much interest owing to its latent high sensitivity and low cost.[3] Recently, many novel photoelectric beacons have been incorporated into PEC bioanalysis, such as core–shell ZnO@MOF heterostructures,[4] Mn:CdS@ZnS,[5] $IrO_2$-Hemin-$TiO_2$ nanowire arrays and NiO nanoflakes-$TiO_2$ nanowire arrays.[6,7] Although these PEC biosensors provided a better analytical performance, their preparation and electrode fabrication were tedious and complicated. Thus, a simple PEC biosensor that can be easily fabricated is still necessary.

Semiconductor doping, particularly metal oxide semiconductor doping with transition metal ions such as $Mn^{2+}$, $Co^{2+}$, $Ni^{2+}$, $Cu^{2+}$, and $Nd^{2+}$,[10–13] has attracted significant attention as a way to introduce new properties.[8,9] On the other hand, ZnO, an excellent host material for doping transition metal ions, has attracted lots of interest as it has a wide direct bandgap, good biocompatibility, and stability. This properties make ZnO an important material in optoelectronic and biosensing applications.[14,15] Therefore, doped ZnO-based photoelectric beacons have great potential as PEC biosensors. Despite this, the number of reports on this type of biosensors is limited.[16]

Herein, Mn-doped ZnO nanorods have been for the first time introduced as a novel photoelectric beacon for label-free PEC aptasensing of potassium ions. Similar to the analogue Co- or Ni-doped ZnO nanowire arrays,[17] the robust Mn-doped ZnO nanorods could be facilely synthesized in a controlled manner by a simple one-pot electrodeposition method.

Given the isoelectric point of about pH 9.5 of the ZnO nanostructure,[18] the negatively charged $K^+$ aptamer could directly self-assemble onto the positively charged surface of Mn-doped ZnO nanorods in phosphate-buffered saline (pH 7.0). In the presence of $K^+$, the G-quadruplex structure of the aptamer can have conformational change to form a $K^+$-stabilized aptamer, which can prevent the electron donor quercetin from arriving at the surface of the functionalized electrode (Scheme 1). Consequently, the enhanced PEC signal in the presence of

[a]Jiangsu Key Laboratory of Biofunctional Materials, College of Chemistry and Materials Science, Nanjing Normal University, Nanjing 210023, P.R. China. E-mail: daizhihuii@njnu.edu.cn; Fax: +86-25-85891051; Tel: +86-25-85891051
[b]College of Chemistry and Chemical Engineering, Yancheng Institute of Technology, Yancheng 224051, P.R. China. E-mail: hbli@ycit.edu.cn

Table 1 Recently reported aptasensors for $K^+$ detection

| Method | Signal material | Linear range | LOD[b] | Ref. |
|---|---|---|---|---|
| Colorimetric | Au NPs | 5 nM–1 μM[a] | 5 nM | 36 |
| Colorimetric | Hairpin DNA | 10 nM–10 mM | 1.9 nM | 1 |
| Colorimetric | Au NPs/DNA enzyme | 0.1–20 mM | 0.1 mM | 37 |
| EIS | $[Fe(CN)_6]^{3-/4-}$ | 0.1 nM–1 mM | 0.1 nM | 29 |
| SWV | Au NPs/$[Fe(CN)_6]^{3-/4-}$ | 10 pM–0.1 μM and 0.5 μM–1 mM | 0.13 pM | 38 |
| CC[c] | MB-labeled hairpin DNA/DNA enzyme | 50 nM–1 mM | 50 nM | 39 |
| *I–t*[d] | HQ/G4 | 5–200 μM | 0.4 μM | 40 |
| FL[e] | CPE/MBA | 5–30 nM | 1.5 nM | 41 |
| FL | DNA-templated Ag NCs | 50–200 μM | 6.2 μM | 42 |
| FL | Zn-DIGP/c-Myc complex | 0.8–10 μM | 0.8 μM | 43 |
| FL | $N^{3+}$ | 0.04–2.0 mM | 0.9 μM | 44 |
| ECL[f] | Au NPs/CdS NCs | 2.0–15 mM | — | 45 |
| PEC[g] | Mn-doped ZnO nanorods array | 0.012–12.32 nM | 4.0 pM | This work |

[a] mM: mmol $L^{-1}$; μM: μmol $L^{-1}$; nM: nmol $L^{-1}$; pM: pmol $L^{-1}$. [b] LOD: limit of detection. [c] CC: chronocoulometry. [d] *I–t* means Amperometric technique. [e] FL: fluorescence. [f] ECL: electrochemiluminescence. [g] PEC: photoelectrochemical.

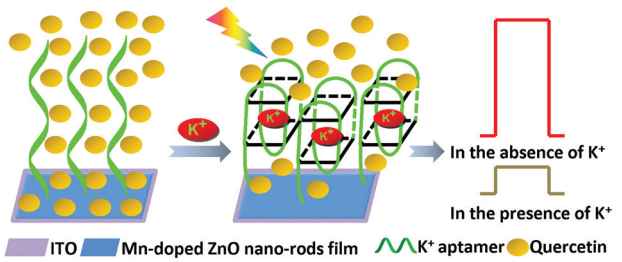


Scheme 1 Schematic with the underlying mechanism of $K^+$ detection by PEC, based on the conformational change of the $K^+$ aptamer.

quercetin proportionately decreased due to the presence of the $K^+$-stabilized G-quadruplex structure on the photoanode surface. The as-fabricated PEC sensor was applied to the detection of $K^+$ in human serum samples, and the results agreed well with those obtained by ICP-MS. The label-free PEC $K^+$ aptasensor demonstrated a good performance in terms of ultrasensitivity, selectivity, simplicity, and had a low cost.

# 2 Experimental

## 2.1 Materials and reagents

The DNA oligonucleotides (Guaranteed Oligos, HPLC-purified) were synthesized by Sangon Biotechnology Co., Ltd (Shanghai, China) and had the following sequence: 5′-GGG TTA GGG TTA GGG TTA GGG-3′ ($K^+$ aptamer).[19] $MnSO_4{\cdot}H_2O$, $Zn(NO_3)_2{\cdot}6H_2O$, $KNO_3$, KCl, NaCl, $Na_2HPO_4$, $NaH_2PO_4$, $MgCl_2{\cdot}6H_2O$, $NH_4NO_3$, $CuSO_4{\cdot}5H_2O$, $ZnSO_4{\cdot}7H_2O$, $Al(NO_3)_3$, $Ca(NO_3)_2{\cdot}4H_2O$ and other chemicals were purchased from Sinopharm Chemical Co., Ltd (Shanghai, China). All reagents were of analytical grade and used directly without purification. In this work, $Na_2HPO_4$ and $NaH_2PO_4$ were used for preparing phosphate-buffered saline (PBS) solutions; 0.1 mol $L^{-1}$ PBS was always used as the electrolyte, and the pH value of PBS solutions was kept at 7.0. Millipore ultrapure water (resistivity ≥18.2 MΩ·cm) was used in all experiments.

## 2.2 Apparatus

PEC measurements were performed with a purpose-built PEC system. Photocurrent was measured by the current–time curve method on a CHI660D electrochemical workstation (CH Instruments, Shanghai, China) with a 250 W tungsten halogen lamp as the irradiation source. The distance between the light source and the photoelectrode was fixed at 10 cm. All experiments for PEC measurements were conducted at room temperature using a conventional three-electrode cell system with a modified ITO substrate (5 mm in diameter, resistivity 10 Ω $sq^{-1}$, Zhuhai Kaivo Electronic Components Co. Ltd, China) as the working electrode, a platinum wire as the auxiliary electrode, and a saturated calomel electrode (SCE) as the reference electrode. Scanning electron microscopy (SEM) analysis was performed using a Hitachi S-4800 scanning electron microscope (Hitachi, Tokyo, Japan). X-ray diffraction (XRD) patterns of ZnO and Mn-doped ZnO nanorods were obtained in the range of $2\theta$ from 20° to 80° by step scanning using the Bruker D8 Advance (super speed) diffractometer (Bruker-AEX, Germany) with Cu Kα radiation ($k$ = 0.15406 nm) operated at 40 kV and 100 mA. UV-vis (UV–Vis) diffuse reflectance spectra were recorded at room temperature with a Cary 5000 UV-Vis spectrophotometer (Varian, USA). Photoluminescence (PL) spectra were recorded at room temperature after excitation with a 325 nm line of He–Cd laser (KIMMON, Japan) using a Labram HR800 (Jobin Yvon, France). Chemical composition and oxidation states were analyzed by X-ray photoelectron spectroscopy (XPS) using a ESCALAB 250 spectrometer (Thermo-VG Scientific, USA) with Mg KR ($h\nu$ of 1253.6 eV) as the excitation source, with ultra-high vacuum generators. The control experiment for the $K^+$ quantification was performed using an Agilent 7500a ICP-MS (Palo Alto, CA, USA).

## 2.3 Mn-doped ZnO nanorods preparation

Preparation of Mn-doped ZnO nanorods by electrodeposition was performed in an electrochemical workstation using a standard three-electrode system, following a published method[20] with some modifications. In detail, before electrodeposition,

an ITO electrode (1 cm × 4 cm) was cleaned with a 50 : 1 : 1 (v/v) mixture of water, ammonia and hydrogen peroxide, and finally washed with ultrapure water and dried in air. Then the Mn-doped ZnO nanorods were electrodeposited (−1.0 V *vs.* Ag/AgCl) at 80 °C for 120 min from 0.5 mmol $L^{-1}$ $Zn(NO_3)_2$ and 0.1 mol $L^{-1}$ $KNO_3$ containing different molar ratio of $MnSO_4$ solution on ITO substrate (5 mm in diameter) in a three-electrode system. Unless otherwise indicated, Mn-doped ZnO refers to 16% Mn-doped ZnO, where 16% is the Mn molar percentage. Subsequently, the as-fabricated Mn-doped ZnO nanorod photoanode was cleaned with ultrapure water and dried at 120 °C for 120 min before constructing the PEC sensor. For the control experiment, ZnO nanorods were prepared as described above by electrodeposition on ITO, but without the addition of $MnSO_4$.

### 2.4 Sensor preparation and detection procedure

The $K^+$ aptamer was immobilized onto the Mn-doped ZnO nanorods *via* a classic self-assembly. Briefly, the Mn-doped ZnO nanorod photoanodes were immersed for 12 h at 25 °C in 1.0 mL buffer solution (0.1 mol $L^{-1}$ PBS + 0.05 mol $L^{-1}$ NaCl) containing the $K^+$ aptamer at a concentration of 1.0 μmol $L^{-1}$, followed by thorough rinsing with 0.1 mol $L^{-1}$ PBS. Subsequently, the Mn-doped ZnO nanorod photoanodes were dipped into 1.0 mL $K^+$ solution of a certain concentration and allowed to react for 5 min at 37 °C. Then, the photoanodes were rinsed with 0.1 mol $L^{-1}$ PBS and abundant water. Finally, the as-fabricated PEC sensor was applied to measure the concentration of $K^+$ in 30 mL of 0.1 mol $L^{-1}$ PBS (pH 7.0) with a certain concentration of quercetin. Photocurrent was measured by the current–time curve method at a bias voltage of 0.2 V *vs.* SCE under irradiation with a 250 W tungsten halogen lamp. Unless otherwise indicated, the concentration of quercetin was kept at an optimal 0.5 μmol $L^{-1}$. Control experiments were conducted following the same procedure, except for the metal ions $Na^+$, $Ca^{2+}$, $Mg^{2+}$, $NH_4^+$, $Al^{3+}$, $Zn^{2+}$, and $Cu^{2+}$.

### 2.5 Application to $K^+$ measurements in real samples

A blood serum sample was collected from a volunteer, centrifuged at 4000 rpm for 5 min, kept at 4 °C overnight and filtered through a 0.45 μm Teflon membrane. Known amounts of 10 nmol $L^{-1}$ KCl solution were added to this filtrate. The serum samples were then diluted to a suitable concentration for the analysis. For method validation, the same serum samples were also analyzed using an Agilent 7500a ICP-MS.

## 3 Results and discussion

### 3.1 Characterization of ZnO nanorods and Mn-doped ZnO nanorod array

Fig. 1(A) and (C) shows the low-magnification FESEM images of undoped and 16% Mn-doped ZnO nanorods. It was observed that the distribution of the nanorods on the ITO substrate was mostly uniform for both samples. Nanorods with a

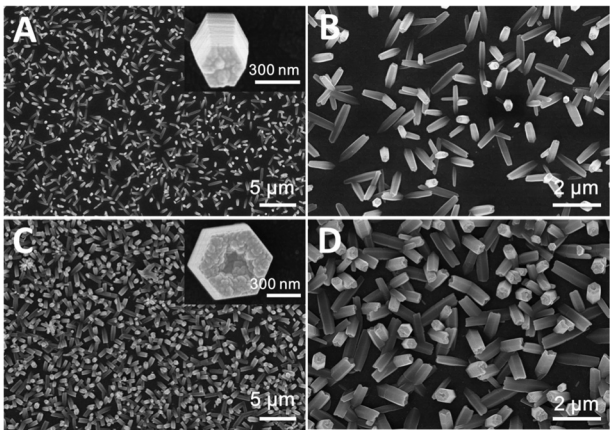


**Fig. 1** Low-magnification (A and C) and high-magnification (B and D) FESEM images of ZnO nanorods (A and B) and 16% Mn-doped ZnO nanorods (C and D) on the ITO substrate. Insets in A and C: high-magnification cross-sectional image.

length and diameter of 1.8 ± 0.2 μm and 300 ± 20 nm (aspect ratio: ~6.0) for undoped nanorods and 1.2 ± 0.2 μm and 600 ± 20 nm (aspect ratio: ~2.0) for Mn-doped nanorods from high-magnification FESEM images can be seen in Fig. 1(B) and (D) and the insets in Fig. 1(A) and (C), respectively. It is obvious that the length of the Mn-doped ZnO nanorods was shorter, which indicated that Mn doping suppressed the axial growth of the ZnO crystals, as could also be concluded from the XRD characterization.

In order to confirm that the transition metal was incorporated into the structure, the XRD patterns of undoped and Mn-doped ZnO nanorod thin films on ITO were recorded (Fig. 2 (A)). All diffraction peaks could be indexed to a pure hexagonal wurtzite structure. The (002) diffraction peak, being the most intense, revealed that the nanorods mainly growed along the [0001] direction.[21] No additional peaks were observed, confirming the phase purity of the ZnO nanorods, which matched very well the standard data (JCPDS, CARD No. 75-1526). No change was observed in the wurtzite structure due to the incorporation of Mn into the ZnO lattice, which indicated that the

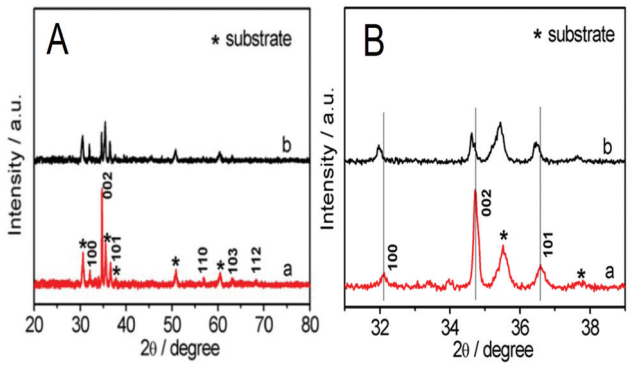


**Fig. 2** (A) XRD patterns of undoped (a) and 16% Mn-doped ZnO nanorods (b), and (B) enlargement of a selected region of the patterns.

presence of Mn does not alter the crystal structure of ZnO. However, for the Mn-doped sample, the main peaks were shifted towards lower diffraction angles (Fig. 2(B)). Furthermore, the lattice constants such as the lattice parameter "a" and "c" as calculated from the (002) diffraction peak of Mn-doped ZnO nanorods were slightly larger, indicating that doping leads to an expansion of the unit cell. Since the effective ionic radius of $Zn^{2+}$ (0.60 Å) is smaller than that of $Mn^{2+}$ (0.66 Å),[22] Mn doping will lead to an expansion of the ZnO lattice and in turn, to a lower diffraction angle, according to the Scherrer equation. Moreover, the relative intensity of the (002) diffraction peak in the pattern of Mn-doped ZnO nanorods is lower than in the pattern of ZnO nanorods, which suggests that Mn atoms may hinder the growth of ZnO nanorods, as observed in the FESEM images (Fig. 1). All these observations indicated that divalent $Mn^{2+}$ ions may replace $Zn^{2+}$ ions within the ZnO crystal lattice, leading to changes in the lattice constants.

XPS spectra provided more direct evidence for the incorporation of doping ions into the host lattice, and also indicated the chemical state of Mn. Fig. 3 shows the XPS survey spectrum of 16% Mn-doped ZnO (A) and the corresponding Zn 2p (B), Mn 2p (C) and O 1s (D) XPS spectra. Spectra were calibrated by taking the carbon C 1s peak as a reference. As expected, peaks ascribed to Zn, Mn, O, mostly displaying the correct binding energies, were observed. As can be seen from Fig. 3(B), two strong peaks appear at 1021.4 and 1044.4 eV, which are in agreement with the binding energies of Zn $2P_{3/2}$ and Zn $2P_{1/2}$, respectively. A spin-orbital splitting of 23.0 eV confirmed that Zn is present as $Zn^{2+}$.[23] Also, the two peaks have narrow line widths (<2 eV), indicating that $Zn^{2+}$ ions are dominant in the nanostructure and the effect of Mn impurities is negligible.[24] Fig. 3(C) shows two broad peaks at 641.1 eV and 655.5 eV, corresponding to Mn $2p_{3/2}$ and Mn $2p_{1/2}$, respectively. The oxidation state of Mn peaked at 639.0 eV, indicating that in our sample the Mn atoms were bonded to other elements.[25] The Mn $2p_{3/2}$ peak indicates the existence of Mn in the Mn(II) state, as in MnO.[26] The peak at 655.5 eV is slightly shifted to a higher binding energy, compared to the binding energy (652.2 eV) reported in other studies on Mn(II).[25,26] This may be attributed to the environmental change caused by Mn(II)-doping in ZnO, and also indicates that there is no simple MnO oxidation state in the doped ZnO sample, as can also be seen from the XRD pattern. In addition, the intensity of the Mn 2p peak in the XPS survey spectrum is very weak Fig. 3(A), which suggests that the content of $Mn^{2+}$ ions at the surface of the sample is very low and that $Mn^{2+}$ ions may have been incorporated within the interior of the nanostructure. The asymmetric O 1s spectrum was coherently fitted by three Gaussian-like components, centered at 529.8, 530.3, and 531.8 eV, as shown in Fig. 3(D). The three peaks above corresponded to $O^{2-}$ ions in the wurtzite structure of the hexagonal $Zn^{2+}$ ion array, $O^{2-}$ ions in oxygen-deficient regions within the ZnO matrix, and $H_2O$ or $O_2$ adsorbed onto the surface, respectively.[24] In summary, the XPS along with the XRD results confirmed that $Mn^{2+}$ ions had been incorporated into the lattice positions of $Zn^{2+}$, and there were no other phases in the samples.

The UV-vis DR and PL spectra of the ZnO and Mn-doped ZnO nanorods are shown in Fig. 4. As shown in Fig. 4(A), the band edge absorption shows a slight red-shift after Mn doping, which is in agreement with other reports.[27] The bandgap shrinkage is interpreted in terms of the s–d and p–d exchange interactions between the band electrons and the localized d electrons of the transition metal ions replacing Zn ions.[28] This band gap shrinkage is beneficial to improve the photoelectric conversion efficiency and thus, the PEC sensitivity. As shown in Fig. 4(B), an evident red-shift of the UV emission peak after Mn doping was also observed, and the obvious hyperchromic effect might be attributed to an enhanced photon absorption.

### 3.2 Enhanced photocurrent response and PEC mechanism

In order to investigate the mechanism of the PEC aptasensor, the PEC responses of the modified Mn-doped ZnO nanorod photoanode were measured. As can be seen in Fig. 5, under a 250 W tungsten halogen lamp irradiation at a bias voltage of 0.2 V, the photocurrent of the ZnO nanorod photoanode was about 1.632 μA (curve a), while the optimal Mn-doped photo-

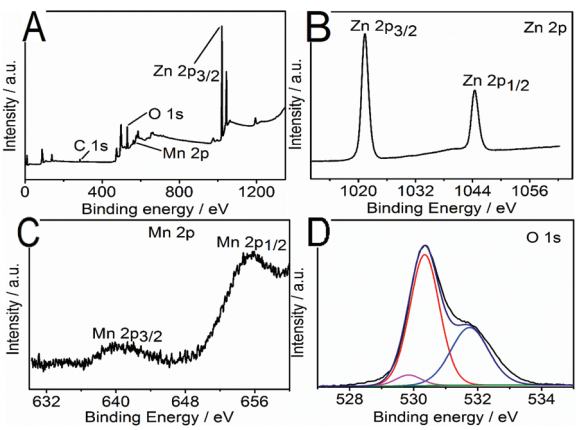


Fig. 3 (A) XPS survey spectrum of 16% Mn-doped ZnO; (B) Zn 2p spectrum; (C) Mn 2p spectrum; (D) O 1s spectrum.

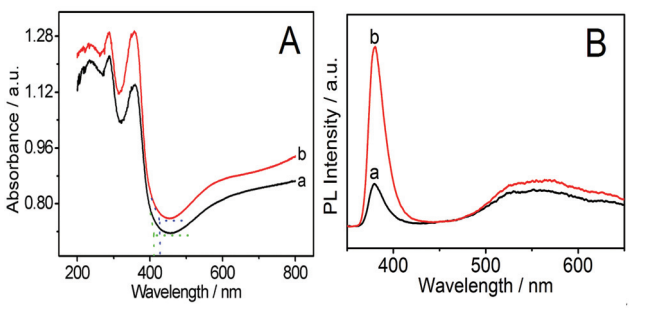


Fig. 4 UV-vis diffuse reflectance (A) and photoluminescence spectra (B) of undoped (a) and 16% Mn-doped ZnO (b) nanorod films.

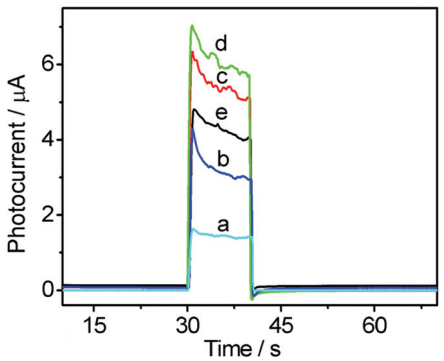


**Fig. 5** Photocurrent response curves of different electrode surfaces in 0.1 mol $L^{-1}$ PBS (pH 7.0) at a bias voltage of 0.2 V *vs.* SCE under a 250 W tungsten halogen irradiation: (a) ZnO nanorods; (b) 16% Mn-doped ZnO nanorods; (c) 16% Mn-doped ZnO nanorods in the presence of 0.5 μmol $L^{-1}$ quercetin; (d) 16% Mn-doped ZnO nanorods modified with the $K^+$ aptamer in the presence of 0.5 μmol $L^{-1}$ quercetin; (e) d system with the addition of 0.2 nmol $L^{-1}$ $K^+$.

anode displayed a photocurrent of approximately 4.241 μA (curve b), representing an almost 1.6-fold increase. Subsequently, the $K^+$ aptamer was allowed to directly self-assemble on the surface of the Mn-doped ZnO nanorod photoanode and the photocurrent of the fabricated aptasensor was measured in the presence of quercetin (curve d). The photocurrent increased by 11%, which may be caused by the oxidation of a few basic groups in the $K^+$ aptamer, in close proximity to the electrode surface. On the other hand, when exposed to 0.2 nmol $L^{-1}$ $K^+$ in the presence of quercetin, the photocurrent decreased by 34%, due to the formation of the $K^+$-stabilized G-quadruplex structure,[29] which may prevent the quercetin molecules from reaching the modified electrode surface (curves d and e). The higher the number of $K^+$-stabilized G-quadruplex aptamers, the higher the steric hindrance preventing quercetin from reaching the electrode surface. Therefore, the $K^+$ concentration could be determined based on the decrease in photocurrent.

Besides morphology changes with respect to undoped ZnO and the corresponding effect on the photocurrent, the enhanced PEC performance of Mn-doped ZnO nanorods could also be attributed to three other reasons. Firstly, Mn creates electronic states in the mid gap region of ZnO, which can result in long-lived charge carriers that boost the efficiency of the charge separation.[30,31] Secondly, Mn-doped ZnO results in a change of the ZnO band gap such that the maximal absorption edge shows a bathochromic shift.[32] Thirdly, the external quantum efficiency of the Mn-doped ZnO nanorod array might also be increased by irradiating with a tungsten halogen light.[33]

### 3.3 Optimization of the experimental conditions

The volume of quercetin solution added to the PEC cell and the Mn content in the electrodeposition solution are two key factors affecting the performance of the aptasensor and therefore, they needed to be optimized. Thus, the Mn-doped ZnO nanorod films with 0%, 8%, 12%, 16%, 20% and 30% (molar percentage) $Mn^{2+}$ were prepared, and their photocurrent response was measured. As shown in Fig. 6(A), the photocurrent in 0.1 mol $L^{-1}$ PBS (pH 7.0) at a bias voltage of 0.2 V under a tungsten halogen lamp irradiation increased until a $MnSO_4$ molar percentage of 16%, and then decreased. Thus, it was concluded that Mn-doped ZnO nanorods favored the separation of photogenerated carriers.[30] However, a too high concentration of Mn ions in ZnO may induce a larger strain in the nanorod crystal lattice,[34] which is disadvantageous for the efficient separation and transfer of photogenerated carriers. On the other hand, Fig. 6(B) shows the effect of adding different volumes (0 μL, 5 μL, 10 μL, 15 μL, 20 μL, 30 μL, 40 μL, 60 μL) of 1 mmol $L^{-1}$ quercetin stock solution on the photocurrent response of the Mn-doped ZnO nanorods modified with the $K^+$ aptamer. The photocurrent response of the photoanode increased until the volume of added quercetin solution reached 15 μL, and then gradually reached a plateau, with a slight decrease of the photocurrent response. The reason for this was explained in our former work.[35] Briefly, quercetin could be oxidized to a quinoid structure and easily adsorbed onto the electrode surface, hindering electron transfer. Therefore, too much quercetin may have an adverse effect. Therefore, 16% Mn-doped ZnO nanorods and a 0.5 μmol $L^{-1}$ quercetin solution were adopted in further experiments.

### 3.4 Analytical performance

Under the optimal experimental conditions, the photocurrent response curves of the Mn-doped ZnO nanorods modified with the $K^+$ aptamer-based photoanode was used to quantify $K^+$ at a bias voltage of 0.2 V under a tungsten halogen lamp irradiation, were used to determine the $K^+$ concentration (Fig. 7).

The decrease in photocurrent ($\Delta I = I_0 - I$, where $I_0$ and $I$ represent the photocurrent produced in the absence and in the presence of $K^+$, respectively) displayed a linear increase as

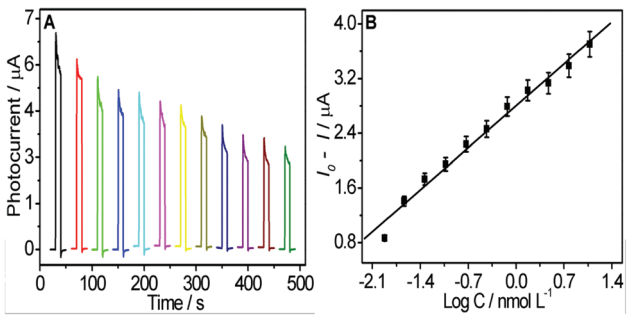


**Fig. 6** (A) Effect of different Mn molar percentages in Mn-doped ZnO nanorod films on the photocurrent response of the Mn-doped ZnO photoanode and (B) effect of different added volumes of 1 mmol $L^{-1}$ quercetin stock solution on the 16% Mn-doped ZnO photoanode modified with the $K^+$ aptamer, both in 30 mL of 0.1 mol $L^{-1}$ PBS (pH 7.0) at a bias voltage of 0.2 V under a tungsten halogen lamp irradiation.

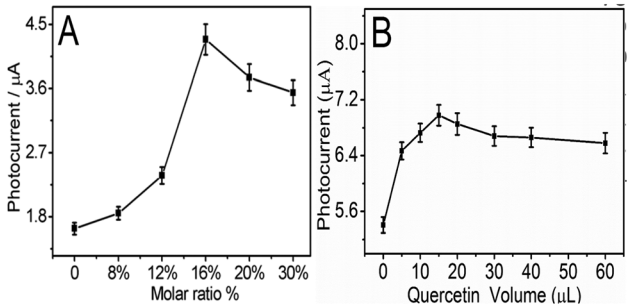


**Fig. 7** Photocurrent responses of 16% Mn-doped ZnO nanorods modified with the $K^+$ aptamer in the presence of 0, 0.012, 0.024, 0.048, 0.096, 0.19, 0.38, 0.77, 1.54, 3.08, 6.16, and 12.32 nmol $L^{-1}$ $K^+$ solution (from left to right) in 0.1 mol $L^{-1}$ pH 7.0 PBS containing 0.5 μmol $L^{-1}$ quercetin at a bias voltage of 0.2 V under a 250 W tungsten halogen lamp irradiation (A) and the corresponding linear calibration curve (B).

the logarithm of $K^+$ concentration increased from 0.012 to 12.32 nmol $L^{-1}$. The limit of detection was 4.0 pmol $L^{-1}$, as determined from the 3$\sigma$/slope, which was 3–5 orders of magnitude lower than that of recently reported methods (Table 1). In comparison to other methods, this PEC $K^+$ aptasensor is a simple, label-free and economical method.

In addition, the PEC $K^+$ aptasensor displayed a good reproducibility in terms of its fabrication, with a relative standard deviation (RSD) of 5.6%, estimated from the slopes of the calibration curves of six freshly prepared 16% Mn-doped ZnO nanorod photoanodes modified with the $K^+$ aptamer. Additionally, the long-term stability of the PEC aptasensor was also investigated. The PEC aptasensors were stored in the refrigerator at 4 °C and photocurrent was measured every 5 days when not in use. After 5 days, no obvious changes were observed in the photocurrent response to potassium ions, and a 94.1% and 92.3% of the initial photocurrent response was retained after 10 and 15 days, respectively. These results indicated that the PEC aptasensor possessed an excellent stability.

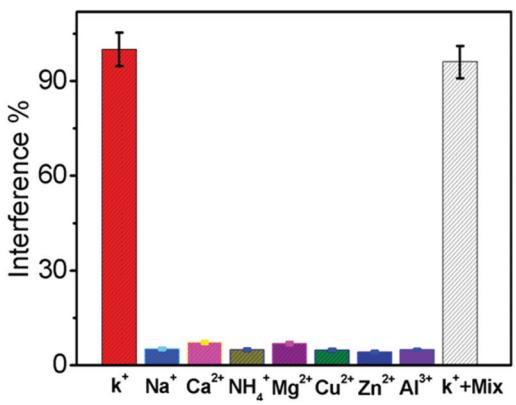


**Fig. 8** Effect of possible interfering ions such as $Na^+$, $Ca^{2+}$, $NH_4^+$, $Mg^{2+}$, $Cu^{2+}$, $Zn^{2+}$, and $Al^{3+}$ at a 10-fold concentration (with respect to $K^+$) on the photocurrent response of Mn-doped ZnO nanorods modified with the $K^+$ aptamer in 0.1 mol $L^{-1}$ PBS (pH 7.0) at a bias voltage of 0.2 V under a 250 W tungsten halogen lamp irradiation.

### 3.5 Interferences selectivity and application to real samples

The selectivity of this system for $K^+$ was evaluated by testing the response towards other common ions at a concentration of 0.2 nmol $L^{-1}$. The results, shown in Fig. 8, indicated that a 10-fold concentration of $Na^+$, $Ca^{2+}$, $NH_4^+$, $Mg^{2+}$, $Cu^{2+}$, $Zn^{2+}$, and $Al^{3+}$ with respect to that of $K^+$ had little effect on the photocurrent response. In addition, a mixture of these ions at the same concentration in a $K^+$ solution did not interfere with the detection of $K^+$. These results demonstrated the excellent specificity of the PEC aptasensor for $K^+$. This excellent selectivity could be attributed to the highly specific interaction of $K^+$ with its aptamer.[19]

The applicability of the PEC aptasensor was demonstrated by measuring the amount of $K^+$ spiked into the blood serum samples of a volunteer. Certain amounts of $K^+$ were added to the real samples and then, after performing the required dilutions and measurements, the recovery values were determined from the calibration curves obtained with the PEC aptasensor and by ICP–MS. As shown in Table 2, both the mean concentration and recovery determined with the sensor were in good agreement with those obtained by ICP–MS, indicating the potential applicability of the PEC aptasensor for the measurement of $K^+$ in human blood serum samples.

## 4 Conclusions

A novel PEC $K^+$ aptasensor was fabricated based on Mn-doped ZnO nanorods and direct self-assembly of the molecular probe. Mn-doped ZnO nanorods were prepared by a one-step electrodeposition and characterized by FESEM, XRD, XPS, UV-Vis and PL. This material was applied to PEC sensing for the first time. Furthermore, the PEC $K^+$ aptasensor exhibited an ultrahigh sensitivity compared to recently reported detec-

**Table 2** Determination of $K^+$ spiked into human blood serum samples using the fabricated PEC aptasensor and by ICP–MS

| Sample | $K^+$ added (mM) | PEC sensor (mM)[a] | Recovery (%) | ICP-MS (mM) | Recovery (%) |
|---|---|---|---|---|---|
| Serum | 0 | 3.82 ± 0.16 | — | 3.89 ± 0.13 | — |
| | 2.00 | 5.71 ± 0.14 | 94.5 | 5.84 ± 0.09 | 97.5 |
| | 4.00 | 7.99 ± 0.12 | 104.3 | 7.71 ± 0.06 | 95.5 |
| | 6.00 | 9.72 ± 0.11 | 98.3 | 10.18 ± 0.08 | 104.8 |

[a] Denotes mean of three measurements ± standard deviation; mM: mmol $L^{-1}$.

 

tion methods. Herein, the biocompatible positively-charged surfaces of the Mn-doped ZnO nanostructures favor the direct self-assembly of the negatively-charged $K^+$ aptamer, without the need to use PDDA or other positively charged polymers as a binder. In comparison to other methods, this $K^+$ aptasensor constitutes a simple detection method, and also saves costs and time, making the sensor more economical. Obviously, the principle described in this work may be applied to other aptamer systems. In summary, this label-free PEC aptasensor is economical, simple, and robust for the ultrasensitive and selective detection of $K^+$ in human serum samples.

## Acknowledgements

This work was supported by the Natural Science Foundation of China (21305123, 21475062, 21505117 and 21625502), the Natural Science Foundation of the Jiangsu Province (BK20161309) and the research fund of the Jiangsu Collaborative Innovation Center for Ecological Building Materials and Environmental Protection Equipments (GX2015103). We appreciate the financial support from the Priority Academic Program Development of the Jiangsu Higher Education Institutions and the Program for the Jiangsu Collaborative Innovation Center of Biomedical Functional Materials.

## Notes and references

1 H. Sun, X. Li, Y. Li, L. Fan and H. B. Kraatz, *Analyst*, 2013, **138**, 856–862.
2 X. Zhou, F. Su, Y. Tian, C. Youngbull, R. H. Johnson and D. R. Meldrum, *J. Am. Chem. Soc.*, 2011, **133**, 18530–18533.
3 W. W. Zhao, J. J. Xu and H. Y. Chen, *Chem. Soc. Rev.*, 2015, **44**, 729–741.
4 W. W. Zhan, Q. Kuang, J. Z. Zhou, X. J. Kong, Z. X. Xie and L. S. Zheng, *J. Am. Chem. Soc.*, 2013, **135**, 1926–1933.
5 Q. Shen, L. Han, G. Fan, J. R. Zhang, L. Jiang and J. J. Zhu, *Anal. Chem.*, 2015, **87**, 4949–4956.
6 J. Tang, B. Kong, Y. C. Wang, M. Xu, Y. L. Wang, H. Wu and G. F. Zheng, *Nano Lett.*, 2013, **13**, 5350–5354.
7 Y. C. Wang, J. Tang, Z. Peng, Y. H. Wang, D. S. Jia, B. Kong, A. A. Elzatahry, D. Y. Zhao and G. F. Zheng, *Nano Lett.*, 2014, **14**, 3668–3673.
8 S. C. Erwin, L. Zu, M. I. Haftel, A. L. Efros, T. A. Kennedy and D. J. Norris, *Nature*, 2005, **436**, 91–94.
9 A. Pandey, S. Brovelli, R. Viswanatha, L. Li, J. M. Pietryga, V. I. Klimov and S. A. Crooker, *Nat. Nanotechnol.*, 2012, **7**, 792–797.
10 T. Dietl, *Nat. Mater.*, 2010, **9**, 965–974.
11 S. B. Ogale, *Adv. Mater.*, 2010, **22**, 3125–3135.
12 D. D. Wang, Q. Chen, G. Z. Xing, J. B. Yi, S. R. Bakaul, J. Ding, J. L. Wang and T. Wu, *Nano Lett.*, 2012, **12**, 3994–4000.
13 J. Kossut, *Nat. Nanotechnol.*, 2012, **7**, 774–775.
14 S. K. Arya, S. Saha, J. E. RamirezVick, V. Gupta, S. Bhansali and S. P. Singh, *Anal. Chim. Acta*, 2012, **737**, 1–21.
15 A. K. Chandiran, M. AbdiJalebi, M. K. Nazeeruddin and M. Grätzel, *ACS Nano*, 2014, **8**, 2261–2268.
16 H. Li, Y. Qiao, J. Li, H. Fang, D. Fan and W. Wang, *Biosens. Bioelectron.*, 2016, **77**, 378–384.
17 J. Cui and U. Gibson, *Appl. Phys. Lett.*, 2005, **87**, 133108.
18 P. Norouzi, V. K. Gupta, F. Faridbod, M. PiraliHamedani, B. Larijani and M. R. Ganjali, *Anal. Chem.*, 2011, **83**, 1564–1570.
19 L. Wang, X. Liu, X. Hu, S. Song and C. Fan, *Chem. Commun.*, 2006, 3780–3782.
20 J. Li, W. W. Tu, H. B. Li, J. C. Bao and Z. H. Dai, *Chem. Commun.*, 2014, **50**, 2108–2110.
21 T. L. Phan and S. C. Yu, *J. Phys. Chem. C*, 2013, **117**, 6443–6453.
22 A. K. Singh, G. S. Thool, P. R. Bangal, S. S. Madhavendra and S. P. Singh, *Ind. Eng. Chem. Res.*, 2014, **53**, 9383–9390.
23 B. Panigrahy, M. Aslam and D. Bahadur, *J. Phys. Chem. C*, 2010, **114**, 11758–11763.
24 L. Yang, X. Wu, G. Huang, T. Qiu and Y. Yang, *J. Appl. Phys.*, 2005, **97**, 014308.
25 P. Ramasamy, S. I. Mamum, J. Jang and J. Kim, *CrystEngComm*, 2013, **15**, 2061–2066.
26 J. Lin, Q. Zhang, L. Wang, X. Liu, W. Yan, T. Wu, X. Bu and P. Feng, *J. Am. Chem. Soc.*, 2014, **136**, 4769–4779.
27 J. Cui and U. Gibson, *Phys. Rev. B: Condens. Matter*, 2006, **74**, 045416.
28 B. Panigrahy, M. Aslam and D. Bahadur, *J. Phys. Chem. C*, 2010, **114**, 11758–11763.
29 Z. B. Chen, L. Chen, H. Ma, T. Zhou and X. X. Li, *Biosens. Bioelectron.*, 2013, **48**, 108–112.
30 P. K. Santra and P. V. Kamat, *J. Am. Chem. Soc.*, 2012, **134**, 2508–2511.
31 Y. Dong, J. Choi, H. K. Jeong and D. H. Son, *J. Am. Chem. Soc.*, 2015, **137**, 5549–5554.
32 L. T. Chang, C. Y. Wang, J. S. Tang, T. X. Nie, W. J. Jiang, C. P. Chu, S. Arafin, L. He, M. Afsal, L. J. Chen and K. L. Wang, *Nano Lett.*, 2014, **14**, 1823–1829.
33 R. R. Prabhakar, N. Mathews, K. B. Jinesh, K. R. G. Karthik, S. S. Pramana, B. Varghese, C. H. Sow and S. Mhaisalkar, *J. Mater. Chem.*, 2012, **22**, 9678–9683.
34 M. Ahmad, E. Ahmed, W. Ahmed, A. Elhissi, Z. L. Hong and N. R. Khalid, *Ceram. Int.*, 2014, **40**, 10085–10097.
35 H. B. Li, J. Li, W. Wang, Z. J. Yang, Q. Xu and X. Y. Hu, *Analyst*, 2013, **138**, 1167–1173.
36 Z. Chen, Y. Huang, X. Li, T. Zhou, H. Ma, H. Qiang and Y. Liu, *Anal. Chim. Acta*, 2013, **787**, 189–192.
37 X. Zhu, J. Zhao, Y. Wu, Z. Shen and G. Li, *Anal. Chem.*, 2011, **83**, 4085–4089.
38 Z. B. Chen, T. H. Zhou, C. M. Zhang, H. Ma, Y. Q. Lin and K. Li, *RSC Adv.*, 2014, **4**, 48671–48675.
39 P. Miao, Y. G. Tang, B. D. Wang, K. Han, X. F. Chen and H. X. Sun, *Analyst*, 2014, **139**, 5695–5699.

40 J. Yu, L. Zhang, X. Xu and S. Liu, *Anal. Chem.*, 2014, **86**, 10741–10748.
41 B. Kim, I. H. Jung, M. Kang, H.-K. Shim and H. Y. Woo, *J. Am. Chem. Soc.*, 2012, **134**, 3133–3138.
42 J. Lee, J. Park, H. H. Lee, H. I. Kim and W. J. Kim, *J. Mater. Chem. B*, 2014, **2**, 2616–2621.
43 H. Qin, J. Ren, J. Wang, N. W. Luedtke and E. Wang, *Anal. Chem.*, 2010, **82**, 8356–8360.
44 W. Yuanboonlim, W. Siripornnoppakhun, N. Niamnont, P. Rashatasakhon, T. Vilaivan and M. Sukwattanasinitt, *Biosens. Bioelectron.*, 2012, **33**, 17–22.
45 L. J. He, M. S. Wu, J. J. Xu and H. Y. Chen, *Chem. Commun.*, 2013, **49**, 1539–1541.